Rapid Communications

X-ray nanodiffraction studies of ionically controlled nanoscale phase separation in cobaltites

Geoffery Rippy,[1] Lacey Trinh,[1] Alexander M. Kane,[1] Aleksey L. Ionin,[1] Michael S. Lee,[1] Rajesh V. Chopdekar,[1] Joyce M. Christiansen-Salameh,[1] Dustin A. Gilbert,[2] Alexander J. Grutter,[3] Peyton D. Murray,[4] Martin V. Holt,[5] Zhonghou Cai,[5,6] Kai Liu,[4,7] Yayoi Takamura,[1] and Roopali Kukreja[1]

[1]*Department of Materials Science and Engineering, University of California Davis, Davis, California 95616, USA*
[2]*Department of Materials Science and Engineering, University of Tennessee, Knoxville, Tennessee 37996, USA*
[3]*NIST Center for Neutron Research, National Institute of Standards and Technology, Gaithersburg, Maryland 20899, USA*
[4]*Department of Physics, University of California Davis, Davis, California 95616, USA*
[5]*Center for Nanoscale Materials, Argonne National Laboratory, Lemont, Illinois 60439, USA*
[6]*Advanced Photon Source, Argonne National Laboratory, Lemont, Illinois 60439, USA*
[7]*Department of Physics, Georgetown University, Washington, DC 20057, USA*

(Received 1 March 2019; revised manuscript received 21 June 2019; published 5 August 2019)

Complex oxide heterostructures provide access to emergent functional and structural phases which are not present in the bulk constituent materials. In this Rapid Communication, we focus on $La_{0.67}Sr_{0.33}CoO_3$ (LSCO)/Gd heterostructures due to the high oxygen ion conductivity, as well as the coupled magnetic and electronic properties of LSCO, which are strongly dependent on the oxygen stoichiometry. This combination of properties enables the ionic control of the functional properties of LSCO thin films through the presence of oxygen getter layers such as Gd. We utilize x-ray nanodiffraction to directly image the nanoscale morphology of LSCO thin films as they are progressively transformed from the equilibrium perovskite phase to the metastable brownmillerite (BM) phase with increasing Gd thickness. Our studies show the coexistence of perovskite and BM phases with a critical oxygen vacancy concentration threshold which leads to the formation of extended BM filaments. In addition to lateral phase separation, we observed phase separation within the film thickness possibly due to pinning of the perovskite and BM phases by the substrate/LSCO and LSCO/Gd interface, respectively. Our studies provide a nanoscale survey of the phase separation in the cobaltites and shed light on the formation of the metastable BM phase.

DOI: 10.1103/PhysRevMaterials.3.082001

Perovskite oxides (ABO_3) exhibit a wide array of tunable functional properties which can be manipulated by tailoring ionic distribution and stoichiometry. Numerous studies have focused on understanding and controlling functionalities via changing the A/B cation stoichiometry in the perovskite structure [1–6]. Recently, there has been a growing interest in utilizing anion stoichiometry [7–13] or substitution, i.e., the formation of oxyfluorides [14,15], to significantly alter and tune the electronic, magnetic, and structural properties. In addition, the presence of the closely related, oxygen-deficient brownmillerite (BM) phase ($ABO_{2.5}$) provides a rich phase diagram with a wide range of functional properties, which are highly sensitive to the oxygen stoichiometry and thus can be tailored via ionic control. Specifically, structural parameters such as BO_6 octahedral bond distances and angles [8,16], as well as electronic parameters such as cation valence states [17,18] are sensitive to the local anion environment and can be modified using epitaxial strain [19,20], external fields [17,21,22] or ionic migration [23]. Large oxygen nonstoichiometry has been demonstrated in $SrCoO_{3-\delta}$ (BM phase), and methods such as oxygen/vacuum anneals, ionic liquids, or electrochemical differences in an electrochemical cell geometry have been utilized to control the oxygen stoichiometry and manipulate functional properties [21,24]. Their highly tunable ionic and electronic transport properties also make them potential candidates for application in devices such as solid oxide fuel cells, information storage, and computing technologies including magnetoionic devices and memristors [25,26].

The deposition of a strong oxygen getter on top of an oxide thin film has recently emerged as a novel way to tailor oxygen stoichiometry and nanoscale functional properties [7,27,28]. For example, the presence of a strong oxygen getter (e.g., Gd) led to the suppression of the magnetization of $La_{0.67}Sr_{0.33}CoO_3$ (LSCO)/Gd heterostructures throughout the full film thickness (36 nm) [27]. In contrast, applying a similar approach to material systems such as (Ni,Co)O/GdFe heterostructures produced a thin (3 nm) layer of ferromagnetic NiCo at the interface [29]. The resulting antiferromagnetic-to-ferromagnetic conversion allowed control of exchange bias at low magnetic fields. In both cases, this phenomenon was associated with the oxidation of the getter layer during which oxygen ions were extracted from the oxide underlayer. The vertical extent of the reaction was postulated to depend on the relative stabilities of the oxide and metal layers, as well as the oxygen ion conductivity and the work function of the getter layer. However, the role played by nanoscale morphology, i.e., phase separation, and defects in these oxide thin films and heterostructures remains largely unknown. High-resolution (scanning) transmission electron microscopy (STEM/TEM) provides a direct method to access atomic lengthscales; however, it is restricted to extremely thin samples (< 10 nm) and

the sample preparation, as well as the imaging process itself, can modify the nanoscale morphology and interfacial properties [30–32]. Thus, while the observation of ordered oxygen vacancies in $La_{1-x}Sr_xCoO_3$ thin films in STEM images can be explained as a means to alleviate epitaxial strain, nondestructive x-ray diffraction–based characterization of long-range oxygen vacancy ordering is still lacking [13,20,33,34].

In this Rapid Communication, we present x-ray nanodiffraction studies to investigate the nanoscale morphology of cobaltite thin films with Gd getter layers. Our nanodiffraction measurements provide an alternative structural characterization method to STEM with nanometer spatial resolution ($\sim$25 nm) in a nondestructive manner to directly image the nanoscale structure [35]. X-ray measurements were performed by tuning to the Bragg reflections which are sensitive to each of the structural rearrangements induced by variations in oxygen stoichiometry of the LSCO film as the Gd layer thickness increases. We observed phase separation of the perovskite and oxygen-deficient BM phases in all samples including the as-grown LSCO reference sample, although the amount of BM phase varied dramatically. For the as-grown sample, we observed a few 0.5–3 μm clusters of the BM phase, while for the LSCO/Gd (0.5 nm) heterostructure, BM clusters grew to lengthscales of 4 μm. Surprisingly, for the LSCO/Gd (3 nm) heterostructure, we observed long filaments in the range of 10–75 μm oriented at either $\sim 10^\circ$ or $\sim 50-60^\circ$ angles from the [100] direction. This result indicates that a critical oxygen vacancy is required to form the BM filaments. Furthermore, in addition to the lateral phase separation, a vertical phase separation is present along the thickness of the film, potentially due to pinning of the perovskite and BM phases by the substrate/LSCO and LSCO/Gd interface, respectively. These results not only advance our understanding of nanoscale morphology in oxides, but also demonstrate a powerful approach to investigate structural and electronic properties at relevant length scales.

Epitaxial $La_{0.67}Sr_{0.33}CoO_3$ (36 nm) thin films were grown by pulsed laser deposition on (001)-oriented $(La_{0.18}Sr_{0.82})(Al_{0.59}Ta_{0.41})O_3$ (LSAT) substrates. The laser energy density utilized for the deposition was 0.9 J/cm^2 at a 1 Hz repetition rate. The samples were deposited at 700 °C with an oxygen pressure of 300 mTorr (40 Pa) and then were slowly cooled to room temperature in 300 Torr (4×10^4 Pa) oxygen pressure. Thin films of elemental Gd (0.5 and 3 nm)/Au (3 nm) were then deposited by sputtering at room temperature in an Ar environment (5 mTorr or 0.67 Pa). Due to the large negative heat of formation (ΔH_f) for GdO_x, the Gd layer spontaneously oxidized upon deposition [36], with the LSCO film acting as the source of the oxygen ions. In order to control the oxygen ion distribution in the LSCO films, two different Gd getter layer thicknesses were deposited (0.5 and 3 nm). The Au layer was deposited before breaking vacuum to prevent oxygen exchange with the ambient environment. Detailed characterization information for these films can be found in Gilbert *et al.* [27].

X-ray nanodiffraction experiments were conducted at the Hard X-ray Nanoprobe (26-ID-C) beamline of the Advanced Photon Source and Center for Nanoscale Materials at Argonne National Laboratory [35,37–39]. Figure 1(a) shows a schematic of the x-ray nanodiffraction experimental

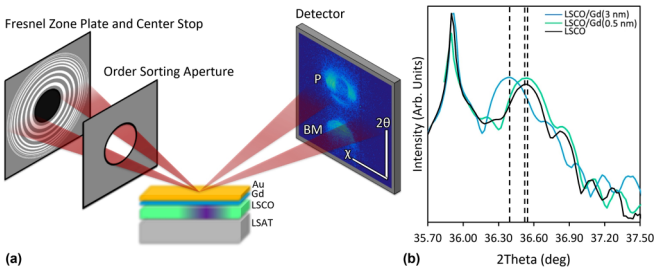

FIG. 1. (a) Schematic of x-ray nanodiffraction experimental setup: Fresnel zone plate focuses x rays down to a 25-nm spot size and the diffracted x rays are collected by a two-dimensional PAD detector. An order-sorting aperture and zone plate central stop are used to block the zero-order x-ray beam. Nanodiffraction images are recorded by scanning the sample. The diffraction pattern captured by the CCD detector shows both $(002)_p$ and $(008)_{bm}$ Bragg reflections for all LSCO/Gd heterostructures. (b) XRD patterns near the $(002)_p$ Bragg reflection for the LSCO/Gd heterostructures and as-grown reference LSCO sample collected using an unfocused x-ray beam.

geometry. The monochromatic (10.4 keV) incident x-ray beam was focused by a Fresnel zone plate down to a 25-nm spot size on the sample. The focusing led to an overall effective beam divergence of 0.24°. A zone plate center stop and order-sorting aperture were used to remove all but the first-order diffracted x-ray beam. As the zone plate center stop blocks the central part of the x-ray beam, the resulting first-order diffracted beam after the zone plate was hollow in the middle. This first-order diffracted x-ray beam was utilized to perform nanodiffraction measurements in a reflection geometry. The diffracted beam from the sample was acquired using a Pixel Area Detector (PAD) detector located 70 cm away from the sample with a pixel size of 55 μm. The sample theta was tuned to access the out-of-plane $(002)_p$ Bragg reflection for the perovskite phase and the $(008)_{bm}$ Bragg reflection for the BM phase simultaneously, thus allowing clear identification of both phases as shown in Fig. 1(a). Here the subscripts p and bm refer to the Miller index notation for the perovskite and BM structures, respectively, and will be used throughout the Rapid Communication. Note that the BM phase is composed of alternating layers of Co ions in octahedral and tetrahedral coordination, resulting in a quadrupling of the unit cell in the c direction in comparison to the parent perovskite phase [2,40]. Therefore, the BM phase can be characterized in an x-ray diffraction (XRD) experiment by a shift of the main film Bragg reflection to lower 2θ values as well as the appearance of half order reflections. Figure 1(b) shows the XRD patterns collected for a macroscopic region near the $(002)_p$ Bragg reflection at 10.4 keV using an unfocused x-ray beam. The shift of main film Bragg reflection to lower 2θ values in Fig. 1(b) and the presence of half order reflections in Ref. [27] indicate that both the BM and perovskite phases are present in LSCO/Gd heterostructures. For the as-grown sample without any metal capping, no shift in the Bragg peak was observed and half order peaks were absent, indicating the presence of only perovskite phase. The out-of-plane lattice parameters obtained for the perovskite phase were 3.799 Å ± 0.002 Å for the as-grown LSCO sample, and 3.802 Å ± 0.002 Å and 3.817 Å ± 0.002 Å for the LSCO/Gd (0.5 nm) and LSCO/Gd (3 nm)

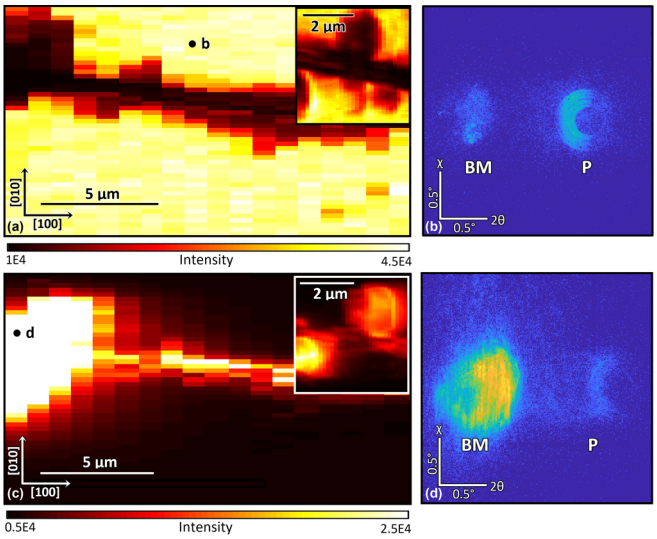

FIG. 2. Nanodiffraction maps for the LSCO/Gd (3 nm) heterostructure: (a) Nanodiffraction map of the integrated intensity of the $(002)_p$ Bragg reflection for the LSCO/Gd (3 nm) heterostructure showing phase separation into perovskite-rich regions (yellow/white) and BM-rich regions (red/brown). The inset image is a zoomed-in map of a section of the feature, showing the complex interface between the two regions. (b) Diffraction pattern at a perovskite-rich region which shows higher intensity of perovskite Bragg reflection compared to the BM Bragg reflection. (c) Nanodiffraction map of the same region, but with the integrated intensity of the $(008)_{bm}$ Bragg reflection. The inset image is the zoomed-in map of the same region as that of the inset in (a). (d) Diffraction pattern at a BM-rich region, showing an increase in intensity of the BM Bragg reflection.

heterostructures, respectively, in agreement with literature values [27]. Unless otherwise noted, all uncertainties represent ±1 standard deviation.

In order to generate high-resolution nanodiffraction maps, the sample was raster scanned using hybrid optomechanical nanopositioning stages [35], recording the diffraction image at each step. The intensity of each pixel of the map represents the integrated intensity on the PAD detector over the given Bragg reflection for a particular sample position (see Supplemental Material [41]). Figure 2(a) shows a nanodiffraction map for the LSCO/Gd (3 nm) heterostructure tuned to the $(002)_p$ Bragg condition. Perovskite-rich regions (yellow/white) are evident by the measured diffraction pattern with higher intensity for the $(002)_p$ reflection as shown in Fig. 2(b). Figure 2(c) shows the same nanodiffraction map but with integrated intensity for the $(008)_{bm}$ Bragg reflection. The reversal of contrast compared to Fig. 2(a) indicates that perovskite-deficient regions indeed consist of BM-rich regions. This fact is also evident by the diffraction pattern shown in Fig. 2(d), where an increase in intensity for the $(008)_{bm}$ Bragg reflection is observed. A zoomed-in scan of the BM filament showing the complex interface between the perovskite and BM phases and the contrast reversal for the integrated intensity in the same region are presented in the insets of Figs. 2(a) and 2(c). These images as well as multiple other nanodiffraction maps (not shown) measured on this sample are consistent with sample-averaged XRD measurements, where Bragg reflections from both perovskite and BM phase are observed indicating that the film is not fully transformed to BM phase. The measured nanodiffraction maps also reveal that even in perovskite-rich regions further away from BM-rich areas, the $(008)_{bm}$ reflection, albeit weak, is still present [Fig. 2(b)]. Similarly, in BM-rich areas, the $(002)_p$ reflection is always observed, revealing that the phase separation exists not only in the lateral direction but also along the film thickness. The presence of both reflections in P- and BM-rich areas was observed in all nanodiffraction scans as well as $\theta/2\theta$ scans (see Supplemental Material [41]). This indicates that the perovskite phase never completely transforms into the BM phase at any given location, and that some BM phase is likely formed everywhere on the sample surface.

Figure 3 compares the nanodiffraction maps for the LSCO/Gd heterostructures as well as the as-grown LSCO reference sample. The LSCO/Gd (0.5 nm) heterostructure shows the presence of BM regions with size ranging from 2 to 4 μm, while for the LSCO/Gd (3 nm) heterostructures, long BM filaments in the range of 10–75 μm were observed as shown in Figs. 3 and 4. For the LSCO/Gd (0.5 nm) heterostructure, only one area showed filament formation and the rest showed similar distribution as Fig. 3(b). In contrast to sample-averaged XRD measurements in Fig. 1(b), even the as-grown LSCO sample showed the presence of BM phase, although the BM regions were fairly scattered across the sample with sizes ranging from 0.5 to 3 μm. These measurements show that the LSCO/Gd (3 nm) heterostructure progressed the furthest in the phase transformation with multiple regions of BM-rich filaments compared to the other samples.

Figure 3(d) presents $\theta/2\theta$ scans for the *local* perovskite- and BM-rich areas for all three samples, measured at the highlighted region in Figs. 3(a)–3(c). The BM phase in the LSCO/Gd (3 nm) heterostructure was highly mosaic and the lattice parameter varied from region to region as confirmed by the shift of the $(008)_{bm}$ Bragg reflection between two different areas [open symbols in Fig. 3(c)]. The variation in the BM lattice parameter ranged from 15.374 Å ± 0.006 Å to 15.358 Å ± 0.006 Å, a difference of 0.016 Å across the sample (in comparison to a difference of 0.013 Å for the perovskite phase within a given sample). Similarly, for the LSCO/Gd (0.5 nm) heterostructure and as-grown LSCO sample, lattice parameters of 15.351 Å ± 0.006 Å and 15.312 Å ± 0.006 Å were obtained for the BM phase resulting in a sample to sample variation of 0.062 Å. In contrast, the sample to sample variation obtained for the perovskite phase is 0.018 Å. As shown in Fig. 3(d), with increasing Gd thickness, the perovskite lattice parameter increases, which is consistent with the incorporation of an increasing concentration of randomly distributed oxygen vacancies and agrees with the trend observed in parallel-beam $\theta/2\theta$ measurements [Fig. 1(b)]. Here we note that while the BM phase and LSAT substrate reflections are close to each other in a sample-averaged XRD pattern, by locally measuring $\theta/2\theta$ scans over the BM phase, we were able to isolate the $(008)_{bm}$ reflection from the substrate as shown in Fig. 3(d), which allowed precise calculation of the BM lattice parameters discussed above.

In order to depict the local changes in the lattice parameter of the perovskite-rich phase, we calculated *c*-axis variation maps for the LSCO/Gd (3 nm) heterostructure as shown in

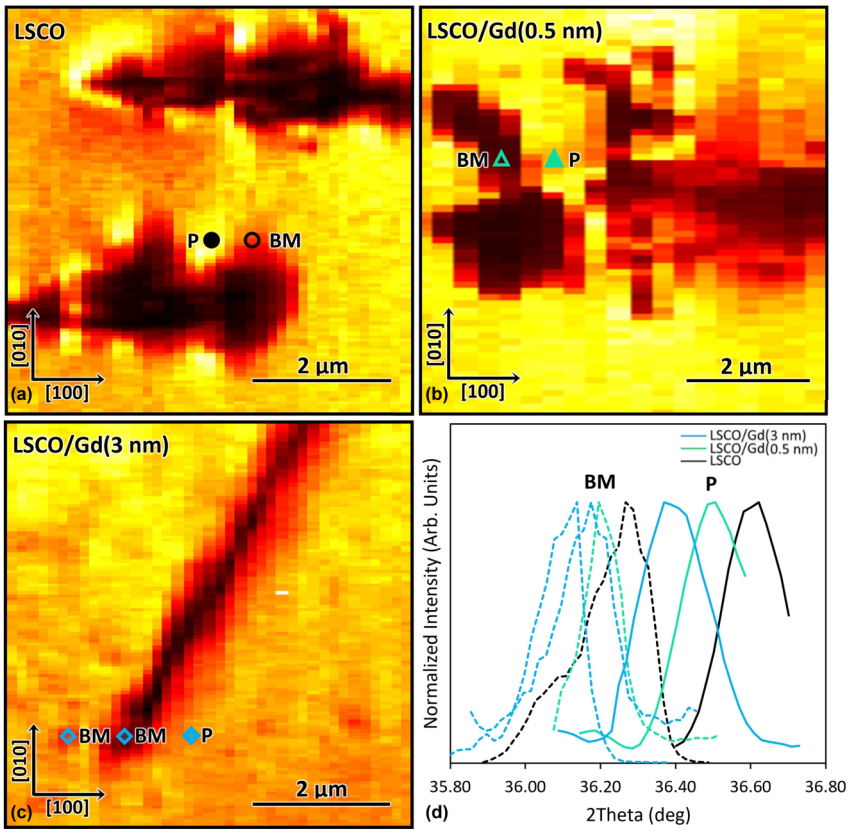

FIG. 3. Comparison of LSCO/Gd heterostructures: Nanodiffraction maps of the integrated intensity of the $(002)_p$ Bragg reflection for LSCO/Gd heterostructures with Gd thicknesses of (a) 0 nm, (b) 0.5 nm, and (c) 3 nm. The yellow regions represent the perovskite-rich phase and red/brown regions indicate BM-rich phase. (d) Local θ-2θ scans from the regions indicated in panels (a), (b), and (c) which allow for the determination of the local lattice parameter for each phase as discussed in the text. The open symbols represent measurements on the BM phase, while closed symbols represent the perovskite phase. A variation in *local* lattice parameter for the BM phase within a given sample is observed as shown for two BM regions in (c), and within the perovskite phase between samples due to the increase in oxygen vacancy concentration as the Gd thickness increases.

Figs. 4(a) and 4(b). The c-axis variation ($\Delta c/c$) is defined as $(c_{x,y} - c_{\text{ref}})/c_{\text{ref}}$, where $c_{x,y}$ is local lattice parameter obtained from nanodiffraction maps, and c_{ref} is the sample-averaged lattice parameter for the perovskite phase calculated by averaging the lattice parameter measured in all nanodiffraction scans for the sample. The average lattice parameters obtained were 3.799 ± 0.002 Å, 3.802 ± 0.002 Å, and 3.811 ± 0.002 Å for the as-grown LSCO, LSCO/Gd (0.5 nm), and LSCO/Gd (3 nm) heterostructures, respectively. The BM phase is also highlighted in the figure and the local c-axis variation for the residual perovskite phase in the BM-rich region is plotted as well. Both maps reveal that the c-axis variation for the perovskite phase switches from positive to negative values on opposite sides of the BM filaments. Figures 4(c) and 4(d) plot line scans adjacent to the BM phase clearly showing this positive to negative reversal in c-axis variation across the BM filament. This sign reversal of the c-axis variation was present consistently in all regions with BM filaments measured for the LSCO/Gd (3 nm) heterostructure. Here we note that this sign reversal depicts the subtle local changes in the lattice parameter of the perovskite phase, which is already under the biaxial strain imposed by the substrate.

The fact that these extended filaments were prominently observed for the LSCO/Gd (3 nm) heterostructure, and were rarely observed in the LSCO/Gd (0.5 nm) heterostructure, as well as their complete absence in the as-grown LSCO sample suggests the presence of a critical local oxygen vacancy concentration in order to achieve growth of long BM filaments. Once the oxygen vacancy concentration exceeds this threshold, small BM clusters grow to form long filaments as observed in the LSCO/Gd (3 nm) heterostructure. A total of seven filaments were measured spread over an approximately $200 \times 200\,\mu\text{m}^2$ region for the LSCO/Gd (3 nm) sample. Four of the seven filaments were oriented at $50^\circ - 60^\circ$ from the $[100]_p$ in-plane direction and the remaining three were oriented at 10° from the $[100]_p$ in-plane direction. In the BM structure, the oxygen vacancies are typically arranged within the BO layer resulting in chains of vacancies parallel to the $[110]_p$ direction of the perovskite lattice. This rearrangement results in chains of apex-linked BO_4 tetrahedra which also are along the $[110]_p$ direction of the perovskite lattice. Distortions to these tetrahedral chains have been observed in $La_{(1-x)}A_xMnO_{2.5}$ as a function of composition and size of cation with deviations in the range of $60^\circ - 70^\circ$ [40]. These tetrahedral chain distortions as well as the fact that we are imaging these vacancy channels in diffraction geometry, i.e., at an angle of about $\sim 20^\circ$ from the sample, can explain the observed orientation of for the BM filaments in the nanodiffraction maps. The presence of BM filaments with an orientation of $\sim 10^\circ$, however, is still puzzling and could potentially imply much higher distortions of the emerging BM phase.

It is also noticeable that the BM phase grows to alleviate the strain in the perovskite phase due to the consistent observation of a change in sign of c-axis variation across the BM filament. Additionally, as discussed above, the perovskite phase never completely transforms into the BM phase at any given location and vice versa. Thus, even in the BM filaments, a small amount of perovskite is present potentially due to pinning of the perovskite phase by the LSAT substrate. Similarly, for the perovskite phase, a small amount of BM phase is always observed which potentially implies a complete depletion of the oxygen in the top LSCO layer, resulting in

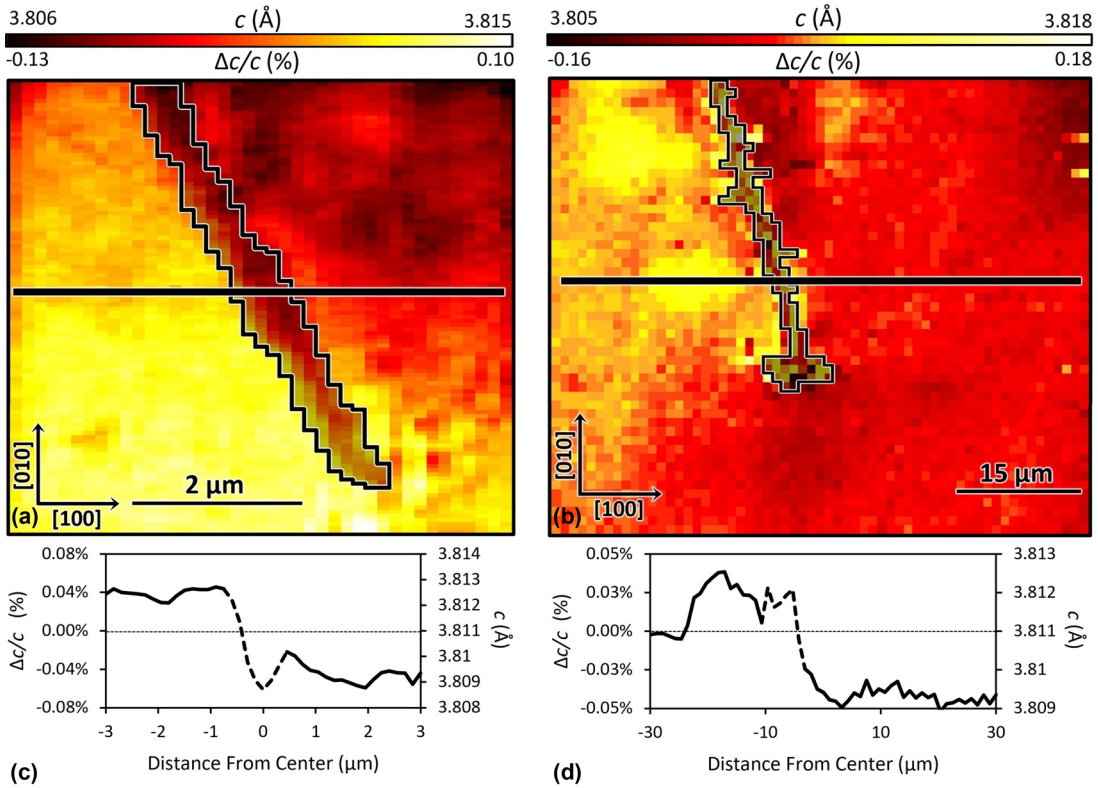

FIG. 4. Local variation of the c-axis lattice parameter in the LSCO/Gd (3 nm) heterostructure: c-axis lattice parameter and c-axis variation maps ($\Delta c/c$, as defined in the text) for the perovskite phase around two BM filaments in the LSCO/Gd (3 nm) heterostructure. These maps show local changes in the c-axis lattice parameter and the c-axis variation of the perovskite phase for (a) a smaller $6 \times 6\,\mu\text{m}^2$ region shown in Figure 3(c), and (b) a larger $80 \times 80\,\mu\text{m}^2$ region. The gray shading highlights the BM filaments. The c-axis variation of the residual perovskite phase present in the BM filaments is also plotted. c-axis variation was calculated using a reference lattice parameter of 3.811 Å, which was determined by averaging multiple nanodiffraction scans as described in text. (c) and (d) show line scans across the BM filament clearly showing the reversal from positive to negative values for the c-axis variation. The dashed (solid) line refers to the calculated values for the perovskite phase present in the BM-rich region (perovskite-rich regions).

the BM transformation at the LSCO/Gd interface throughout the surface area of the LSCO film. These measurements thus allow us to not only discern and image the phase separation in LSCO/Gd heterostructures laterally, but also provide indication of phase separation across the thin film depth.

In summary, our x-ray nanodiffraction measurements shed light on the structural transformation in LSCO heterostructures as a function of Gd getter layer thickness in a nondestructive manner. This transformation proceeds by phase separation, resulting in an evolution of the lateral distribution of the perovskite and BM phases with Gd thickness. Phase separation across the depth is also observed which could be potentially due to pinning of the perovskite or BM phase at the LSCO/substrate and LSCO/Gd interface, respectively. Above a critical thickness of Gd layer (3 nm), long BM filaments are observed due to ordering of oxygen vacancies at $50^\circ - 60^\circ$ or 10° angles from the $[100]_p$ direction. The emerging BM phase is highly distorted as observed by the deviations of tetrahedral chains from the $[110]_p$ directions, high mosaicity, and variations in lattice parameter of 0.04 Å. The perovskite phase shows a change in the local c-axis parameter on opposite sides of the BM filaments. These measurements highlight local structural effects in LSCO/Gd heterostructures and provide insights regarding nanoscale strain behavior near phase boundaries. Manipulation of these nanoscale heterogeneities, i.e., BM filaments, by varying getter layer or electric field can provide a unique method to tailor the electronic and ionic conductivity in an ionically gated device. These nanoscale filaments can provide channels across which oxygen ion conduction can occur without the need of bulk structural transformation and thus will be more energetically favorable. Reversible control of these filaments will open new avenues of controlling anion conduction in applications such as solid oxide fuel cells and magnetoionic devices.

G.R., L.T., J.M.C.-S., and R.K. acknowledge the support by University of California Davis for this research while A.M.K., A.L.I., M.S.L., R.V.C., and Y.T. acknowledge the University of California Multicampus Research Programs and Initiatives (Grant No. MR-15-328528). P.D.M and K.L. acknowledge support from the NSF (ECCS-1611424 and DMR-1905468). This research used resources of the Advanced Photon Source and the Center for Nanoscale Materials, both U.S. Department of Energy (DOE) Office of Science User Facilities operated for the DOE Office of Science by Argonne National Laboratory under Contract No. DE-AC02-06CH11357.

[1] J. Wu and C. Leighton, Glassy ferromagnetism and magnetic phase separation in $La_{1-x}Sr_xCoO_3$, Phys. Rev. B **67**, 174408 (2003).

[2] E. Dixon, J. Hadermann, and M. A. Hayward, The synthesis and complex anion-vacancy ordered structure of $La_{0.33}Sr_{0.67}MnO_{2.42}$, J. Solid State Chem. **184**, 1791 (2011).

[3] N. Setter and L. E. Cross, The role of B-site cation disorder in diffuse phase transition behavior of perovskite ferroelectrics, J. Appl. Phys. **51**, 4356 (1980).

[4] A. S. Ogale, S. B. Ogale, R. Ramesh, and T. Venkatesan, Octahedral cation site disorder effects on magnetization in double-perovskite Sr_2FeMoO_6: Monte Carlo simulation study, Appl. Phys. Lett. **75**, 537 (1999).

[5] T. Nagai, W. Ito, and T. Sakon, Relationship between cation substitution and stability of perovskite structure in $SrCoO_{3-\delta}$-based mixed conductors, Solid State Ionics **177**, 3433 (2007).

[6] R. Caciuffo and D. Rinaldi, G. Barucca, J. Mira, J. Rivas, M. A. Señarís-Rodríguez, P. G. Radaelli, D. Fiorani, and J. B. Goodenough, Structural details and magnetic order of $La_{1-x}Sr_xCoO_3$ ($x \leqslant 0.3$), Phys. Rev. B **59**, 1068 (1999).

[7] J. D. Ferguson, Y. Kim, L. F. Kourkoutis, A. Vodnick, A. R. Woll, D. A. Muller, and J. D. Brock, Epitaxial oxygen getter for a brownmillerite phase transformation in manganite films, Adv. Mater. **23**, 1226 (2011).

[8] H. Jeen, W. S. Choi, H. W. Freeland, H. Ohta, C. U. Jung, and H. N. Lee, Topotactic phase transformation of the brownmillerite $SrCoO_{2.5}$ to the perovskite $SrCoO_{3-\delta}$, Adv. Mater. **25**, 3651 (2013).

[9] A. L. Krick and S. J. May, Evidence for oxygen vacancy manipulation in $La_{1/3}Sr_{2/3}FeO_{3-\delta}$ thin films via voltage controlled solid-state ionic gating, APL Mater. **5**, 042504 (2017).

[10] A. Kalabukhov, R. Gunnarsson, J. Börjesson, E. Olsson, T. Claeson, and D. Winkler, Effect of oxygen vacancies in the $SrTiO_3$ substrate on the electrical properties of the $LaAlO_3/SrTiO_3$ interface, Phys. Rev. B **75**, 121404(R) (2007).

[11] R. I. Dass, J.-Q. Yan, and J. B. Goodenough, Oxygen stoichiometry, ferromagnetism, and transport properties of $La_{2-x}NiMnO_{6+\delta}$, Phys. Rev. B **68**, 064415 (2003).

[12] M. D. Biegalski, E. Crumlin, A. Belianinov, E. Mutoro, Y. Shao-Horn, and S. V. Kalinin, *In situ* examination of oxygen non-stoichiometry in $La_{0.80}Sr_{0.20}CoO_{3-\delta}$ thin films at intermediate and low temperatures by x-ray diffraction, Appl. Phys. Lett. **104**, 161910 (2014).

[13] J. Gazquez, Shameek Bose, M. Sharma, M. A. Torija, S. J. Pennycook, C. Leighton, and M. Varela, Lattice mismatch accommodation via oxygen vacancy ordering in epitaxial $La_{0.5}Sr_{0.5}CoO_{3-\delta}$ thin films, APL Mater. **1**, 012105 (2013).

[14] E. J. Moon, Y. Xie, E. D. Laird, D. J. Keavney, C. Y. Li, and S. J. May, Fluorination of epitaxial oxides: Synthesis of perovskite oxyfluoride thin films, J. Am. Chem. Soc. **136**, 2224 (2014).

[15] E. J. Moon, A. K. Choquette, A. Huon, S. Z. Kulesa, D. Barbash, and S. J. May, Comparison of topotactic fluorination methods for complex oxide films, APL Mater.s **3**, 062511 (2015).

[16] J. B. Torrance, P. Lacorre, A. I. Nazzal, E. J. Ansaldo, and C. Niedermayer, Systematic study of insulator-metal transitions in perovskites $RNiO_3$ (R = Pr, Nd, Sm, Eu) due to closing of charge-transfer gap, Phys. Rev. B **45**, 8209(R) (1992).

[17] N. Lu, P. Zhang, Q. Zhang, R. Qiao, Q. He, H.-B. Li, Y. Wang, J. Guo, D. Zhang, Z. Duan *et al.*, Electric-field control of tri-state phase transformation with a selective dual-ion switch, Nature (London) **546**, 124 (2017).

[18] Y. Moritomo, Y. Tomioka, A. Asamitsu, Y. Tokura, and Y. Matsui, Magnetic and electronic properties in hole-doped manganese oxides with layered structures: $La_{1-x}Sr_{1+x}MnO_4$, Phys. Rev. B **51**, 3297(R) (1995).

[19] D. Fuchs, E. Arac, C. Pinta, S. Schuppler, R. Schneider, and H. v. Löhneysen, Tuning the magnetic properties of $LaCoO_3$ thin films by epitaxial strain, Phys. Rev. B **77**, 014434 (2008).

[20] W. S. Choi, J.-H. Kwon, H. Jeen, J. E. Hamann-Borrero, A. Radi, S. Macke, R. Sutarto, F. He, G. A. Sawatzky, V. Hinkov *et al.*, Strain-induced spin states in atomically ordered cobaltites, Nano Lett. **12**, 4966 (2012).

[21] Q. Lu and B. Yildiz, Voltage-controlled topotactic phase transition in thin-film $SrCoO_x$ monitored by *in situ* x-ray diffraction, Nano Lett. **16**, 1186 (2016).

[22] J. Walter, G. Yu, B. Yu, A. Grutter, B. Kirby, J. Borchers, Z. Zhang, H. Zhou, T. Birol, M. Greven *et al.*, Ion-gel-gating-induced oxygen vacancy formation in epitaxial $La_{0.5}Sr_{0.5}CoO_{3-\delta}$ films from *inoperando* x-ray and neutron scattering, Phys. Rev. Mater. **1**, 071403 (2017).

[23] B. Cui, P. Werner, T. Ma, X. Zhong, Z. Wang, J. M. Taylor, Y. Zhuang, and S. S. P. Parkin, Direct imaging of structural changes induced by ionic liquid gating leading to engineered three-dimensional meso-structures, Nat. Commun. **9**, 3055 (2018).

[24] H. Jeen, W. S. Choi, M. D. Biegalski, C. M. Folkman, I-Cheng Tung, D. D. Fong, J. W. Freeland, D. Shin, H. Ohta, M. F. Chisholm *et al.*, Reversible redox reactions in an epitaxially stabilized $SrCoO_x$ oxygen sponge, Nat. Mater. **12**, 1057 (2013).

[25] Y.-M. Kim, J. He, M. D. Biegalski, H. Ambaye, V. Lauter, H. M. Christen, S. T. Pantelides, S. J. Pennycook, S. V. Kalinin, and A. Y. Borisevich, Probing oxygen vacancy concentration and homogeneity in solid-oxide fuel-cell cathode materials on the subunit-cell level, Nat. Mater. **11**, 888 (2012).

[26] J. J. Yang, M. D. Pickett, X. Li, D. A. A. Ohlberg, D. R. Stewart, and R. S. Williams, Memristive switching mechanism for metal/oxide/metal nanodevices, Nat. Nanotechnol. **3**, 429 (2008).

[27] D. A. Gilbert, A. J. Grutter, P. D. Murray, R. V. Chopdekar, A. M. Kane, A. L. Ionin, M. S. Lee, S. R. Spurgeon, B. J. Kirby, B. B. Maranville *et al.*, Ionic tuning of cobaltites at the nanoscale, Phys. Rev. Mater. **2**, 104402 (2018).

[28] A. J. Grutter, D. A. Gilbert, U. S. Alaan, E. Arenholz, B. B. Maranville, J. A. Borchers, Y. Suzuki, K. Liu, and B. J. Kirby, Reversible control of magnetism in $La_{0.67}Sr_{0.33}MnO_3$ through chemically-induced oxygen migration, Appl. Phys. Lett. **108**, 082405 (2016).

[29] D. A. Gilbert, J. Olamit, R. K. Dumas, B. J. Kirby, A. J. Grutter, B. B. Maranville, E. Arenholz, J. A. Borchers, and K. Liu, Controllable positive exchange bias via redox-driven oxygen migration, Nat. Commun. **7**, 11050 (2016).

[30] L. Yao, S. Majumdar, L. Äkäslompolo, S. Inkinen, Q. H. Qin, and S. van Dijken, Electron-beam-induced perovskite-brownmillerite-perovskite structural phase transitions in epitaxial $La_{2/3}Sr_{1/3}MnO_3$ films, Adv. Mater. **26**, 2789 (2014).

[31] V. Srot, M. Gec, P. A. van Aken, J.-H. Jeon, and M. Čeh, Influence of TEM specimen preparation on chemical composition of $Pb(Mg_{1/3}Nb_{2/3})O_3-PbTiO_3$ single crystals, Micron **62**, 37 (2014).

[32] E. Eberg, Å. F. Monsen, T. Tybell, A. T. J. van Helvoort, and R. Holmestad, Comparison of TEM specimen preparation of perovskite thin films by tripod polishing and conventional ion milling, J. Electron Microsc. (Tokyo) **57**, 175 (2008).

[33] M. Sharma, J. Gazquez, M. Varela, J. Schmitt, and C. Leighton, Coercivity enhancement driven by interfacial magnetic phase separation in $SrTiO_3(001)/Nd_{0.5}Sr_{0.5}CoO_3$, Phys. Rev. B **84**, 024417 (2011).

[34] J. Walter, S. Bose, M. Cabero, G. Yu, M. Greven, M. Varela, and C. Leighton, Perpendicular magnetic anisotropy via strain-engineered oxygen vacancy ordering in epitaxial $La_{1-x}Sr_xCo_{3-\delta}$, Phys. Rev. Mater. **2**, 111404 (2018).

[35] S. O. Hruszkewycz, M. V. Holt, J. Maser, C. E. Murray, M. J. Highland, C. M. Folkman, and P. H. Fuoss, Coherent Bragg nanodiffraction at the hard X-ray Nanoprobe beamline, Philos. Trans. R. Soc., A **372**, 20130118 (2014).

[36] A. B. Posadas, K. J. Kormondy, W. Guo, P. Ponath, J. Geler-Kremer, T. Hadamek, and A. A. Demkov, Scavenging of oxygen from $SrTiO_3$ during oxide thin film deposition and the formation of interfacial 2DEGs, J. Appl. Phys. **121**, 105302 (2017).

[37] R. P. Winarski, M. V. Holt, V. Rose, P. Fuesz, D. Carbaugh, C. Benson, D. Shu, D. Kline, G. B. Stephenson, I. McNulty, and J. Maser, A hard X-ray nanoprobe beamline for nanoscale microscopy, J. Synchrotron Radiat. **19**, 1056 (2012).

[38] M. Holt, R. Harder, R. Winarski, and V. Rose, Nanoscale hard x-ray microscopy methods for materials studies, Annu. Rev. Mater. Res. **43**, 183 (2013).

[39] S. O. Hruszkewycz, M. V. Holt, M. Allain, V. Chamard, S. M. Polvino, C. E. Murray, and P. H. Fuoss, Efficient modeling of Bragg coherent x-ray nanobeam diffraction, Opt. Lett. **40**, 3241 (2015).

[40] T. G. Parsons, Hans D'Hondt, J. Hadermann, and M. A. Hayward, Synthesis and structural characterization of $La_{1-x}A_xMnO_{2.5}$ (A = Ba, Sr, Ca) phases: Mapping the variants of the brownmillerite structure, Chem. Mater. **21**, 5527 (2009).

[41] See Supplemental Material at http://link.aps.org/supplemental/10.1103/PhysRevMaterials.3.082001 for a brief description of the method utilized for generating nanodiffraction maps, and additional nanodiffraction maps as well as diffraction patterns.